

A Dual-Domain Convolutional Network for Hyperspectral Single-Image Super-Resolution

Murat Karayaka, Usman Muhammad, Jorma Laaksonen, Md Ziaul Hoque and Tapio Seppänen

Abstract—This study presents a lightweight dual-domain super-resolution network (DDSRNet) that combines Spatial-Net with the discrete wavelet transform (DWT). Specifically, our proposed model comprises three main components: (1) a shallow feature extraction module, termed Spatial-Net, which performs residual learning and bilinear interpolation; (2) a low-frequency enhancement branch based on the DWT that refines coarse image structures; and (3) a shared high-frequency refinement branch that simultaneously enhances the LH (horizontal), HL (vertical), and HH (diagonal) wavelet subbands using a single CNN with shared weights. As a result, the DWT enables subband decomposition, while the inverse DWT reconstructs the final high-resolution output. By doing so, the integration of spatial- and frequency-domain learning enables DDSRNet to achieve highly competitive performance with low computational cost on three hyperspectral image datasets, demonstrating its effectiveness for hyperspectral image super-resolution. The source codes are publicly available at: <https://github.com/mkarayak24/DDSRNet>

Index Terms—Remote-sensing, hyperspectral imaging, super-resolution, wavelet domain.

I. INTRODUCTION

Hyperspectral images (HSIs) provide rich spectral information but are limited in spatial resolution due to hardware constraints, while multispectral images (MSIs) achieve higher spatial resolution with fewer spectral bands [1]. Single image super-resolution (SR) aims to reconstruct a high-resolution (HR) image from a low-resolution (LR) observation. Earlier SR methods predominantly used interpolation techniques such as nearest-neighbor, bilinear, and bicubic interpolation [2]. Although computationally efficient and well suited to the hardware of their time, these approaches operated purely on pixel-level computations without incorporating contextual or prior information, resulting in HR images that often lacked fine structural details [1].

In recent years, deep learning-based methods have become dominant in the remote sensing domain [3], [4], [5], [6], especially in super-resolution tasks, [7], [8], demonstrating remarkable improvements in both reconstruction accuracy and perceptual quality. In particular, single-image super-resolution methods have become more popular compared to fusion-based approaches which require an additional RGB or panchromatic image [9]. The main reason is that single-image super-resolution methods are more practical for real-

Manuscript created Dec, 2025; This research work is financially supported by the Center for Machine Vision and Signal Analysis, University of Oulu, Finland.

M. Karayaka, M.Z. Hoque and T. Seppänen are with Center for Machine Vision and Signal Analysis, University of Oulu. Usman Muhammad and Jorma Laaksonen are with the Department of Computer Science, Aalto University, Espoo, Finland.

time deployment. Thus, single-image super-resolution methods have received increased attention in the literature. For instance, a lightweight depthwise separable dilated convolutional neural network that integrates mean squared error (MSE) along with spectral angle-based loss functions was proposed in [10]. Meanwhile, a spectral–spatial fusion approach that employs an Inception-inspired architecture followed by a dedicated multi-scale fusion block has been introduced in [11]. However, the depthwise separable dilated network may suffer from limited global context and spectral distortion, while the Inception-like fusion model introduces higher computational complexity and risks of overfitting on small datasets.

To enhance both spatial resolution and spectral integrity, a plug-and-play module called spectral–spatial unmixing fusion (SSUF) was proposed in [12]. The channel-attention-based spatial–spectral feature extraction network was found to be highly effective in preserving spectral fidelity, as reported in [13]. A spatial–spectral interactive Transformer (SSIT) block integrated into both the encoder and decoder of a U-Net architecture was employed in [14]. Furthermore, a novel Group-Autoencoder (GAE) framework combined with a diffusion model to construct high-quality images was introduced in [15]. However, these methods often suffer from high computational complexity and require extensive training data to achieve stable performance.

We are motivated by the observation that low-frequency components (e.g., smooth structures and global intensity variations) and high-frequency components (e.g., edges and fine textures) exhibit fundamentally different characteristics [16]. Conventional CNNs often process these components together in the spatial domain, which can result in blurred edges or over-smoothing. By transforming the upsampled features into the wavelet domain, we can explicitly separate these components, thereby improving reconstruction quality while reducing computational cost. Therefore, we propose a lightweight dual-domain super-resolution network (DDSRNet) for hyperspectral single image super resolution that combines Spatial-Net with the discrete wavelet transform (DWT).

Specifically, the purpose of the Spatial-Net is to extract and enhance spatial features from the low-resolution input, providing a strong spatial representation for subsequent wavelet-domain refinement. It learns structural and contextual cues such as edges, shapes, and textures, which are crucial for preserving spatial fidelity in the reconstructed high-resolution image. On the other hand, the purpose of the Discrete Wavelet Transform (DWT) is to decompose the feature maps into low- and high-frequency components, allowing the network to process smooth structures and fine textures separately. This

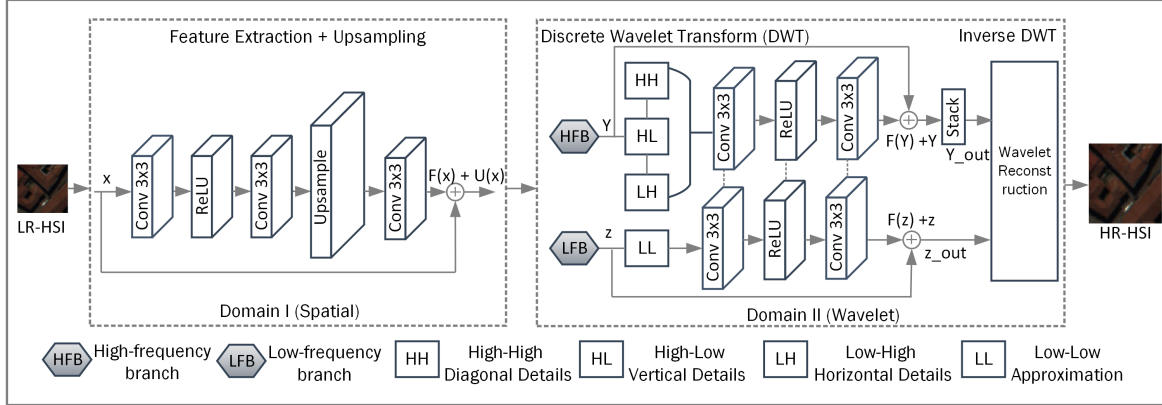


Fig. 1: An overview of the proposed DDSRNet model. The left block represents the first domain, i.e., the Spatial-Net, while the right block illustrates the procedure of the Discrete Wavelet Transform (DWT).

separation helps preserve edge details, reduce over-smoothing, and improve the overall reconstruction quality of the hyper-spectral image. Finally, a hybrid loss function is designed that combines the reconstruction loss in the image domain with auxiliary losses computed in the wavelet and the spatial domains.

In summary, the contributions of this work are summarized as:

- 1) We present a novel dual-domain model, called DDSR-Net, that operates in both the spatial and wavelet domains, with each component designed to be lightweight and suitable for real-time deployment.
- 2) We employ a hybrid loss function that jointly optimizes spatial reconstruction and frequency-domain consistency.
- 3) Experiments conducted on three hyperspectral datasets under $2\times$, $4\times$, and $8\times$ downsampling scenarios demonstrate that the proposed method achieves highly competitive performance across all cases.

II. METHODOLOGY

Fig. 1 illustrates the overall architecture of the proposed DDSRNet model, which comprises two key components: (1) a Spatial-Net that performs initial feature learning, and (2) a Wavelet Decomposition (DWT) module that refines the reconstruction through frequency-domain processing. We first describe the Spatial-Net operating in the spatial domain, followed by the Discrete Wavelet Transform (DWT) module in the frequency domain. The subsequent sections provide a detailed analysis of each component, along with the proposed hybrid loss function used to optimize the overall model.

A. Spatial-Net

The Spatial-Net consists of two successive convolutional layers with ReLU activation, a non-learnable bilinear upsampling layer, and a final projection convolution.

Mathematically, given an input tensor $X \in \mathbb{R}^{B \times C \times H \times W}$, where B is the batch size, C the number of channels, and $H \times W$ the spatial size, Spatial-Net computes:

$$F = \text{Conv}_2(\sigma(\text{Conv}_1(X))), \quad (1)$$

where $F \in \mathbb{R}^{B \times C_h \times H \times W}$ is the low-resolution feature map after two convolutions. $\sigma(\cdot)$ denotes the ReLU function. Similarly, we then apply bilinear upsampling followed by a 3×3 convolution:

$$Y_{\text{main}} = \text{Conv}_3(U(F)), \quad (2)$$

where $U(\cdot)$ is bilinear upsampling by factor s , and $Y_{\text{main}} \in \mathbb{R}^{B \times C \times sH \times sW}$ is the learned high-resolution path output, and C_h is the hidden width:

$$\hat{Y} = Y_{\text{main}} + U(X), \quad \hat{Y} \in \mathbb{R}^{B \times C \times sH \times sW}. \quad (3)$$

where \hat{Y} denotes the Spatial-Net output, and $U(X) \in \mathbb{R}^{B \times C \times sH \times sW}$ is the bilinear skip connection.

B. Discrete Wavelet Decomposition (DWT)

After the image is processed by the Spatial-Net, we apply a discrete wavelet transform (DWT) to decompose the upsampled feature map into low and high frequency components [16]. This process explicitly separates global structural information from fine textures, allowing the network to learn more effective refinements for both components. In our implementation, the DWT is performed using the Haar wavelet, which applies separable low-pass and high-pass filtering along both spatial dimensions, followed by downsampling.

Mathematically, let $\mathbf{X}_\uparrow \in \mathbb{R}^{B \times C \times sH \times sW}$ denote the upsampled input, where B is the batch size, C is the number of channels, and (sH, sW) are the spatial dimensions after upsampling. The 2-D DWT produces one low-frequency subband \mathbf{Y}_{LL} and three high-frequency subbands \mathbf{Y}_{LH} , \mathbf{Y}_{HL} , and \mathbf{Y}_{HH} , obtained as [16]:

$$\mathbf{Y}_{\text{LL}}, \mathbf{Y}_{\text{LH}}, \mathbf{Y}_{\text{HL}}, \mathbf{Y}_{\text{HH}} = \text{DWT}(\mathbf{X}_\uparrow) \quad (4)$$

where \mathbf{Y}_{LL} represents the coarse, low-pass features, while \mathbf{Y}_{LH} , \mathbf{Y}_{HL} , and \mathbf{Y}_{HH} capture vertical, horizontal, and diagonal high-frequency components, respectively. The resulting tensors have dimensions $[B, C, H_d, W_d]$ for \mathbf{Y}_{LL} and $[B, C, 3, H_d, W_d]$ for the stacked high-frequency components, where $H_d = \frac{sH_0}{2}$ and $W_d = \frac{sW_0}{2}$, with H_0 and W_0 denoting the original input height and width, respectively.

In the model, the low-frequency subband \mathbf{Y}_{LL} is processed by a low frequency branch (LFB), which refines smooth regions and overall image structure using residual convolutional layers. Meanwhile, the high-frequency branch (HFB), represented as $\mathbf{Y}_H = [\mathbf{Y}_{LH}, \mathbf{Y}_{HL}, \mathbf{Y}_{HH}]$, is enhanced by a shared Wavelet Branch, where each subband is refined through a small convolutional block with a residual connection to restore textures and sharpen edges. This design allows the model to learn orientation-specific features in the wavelet domain efficiently.

Finally, the reconstructed image is obtained via the inverse wavelet transform (IDWT):

$$\mathbf{X}_{SR} = IDWT(\mathbf{Y}_{LL}^*, \mathbf{Y}_H^*). \quad (5)$$

where \mathbf{Y}_{LL}^* and \mathbf{Y}_H^* are the refined low-frequency and high-frequency feature maps. This explicit frequency separation and recombination improve edge fidelity and structural consistency while minimizing oversmoothing in the reconstructed high-resolution output.

C. Hybrid Loss Function

A hybrid loss function is employed to jointly guide spatial- and frequency-domain learning by combining image-domain reconstruction loss with auxiliary spatial and wavelet losses. Specifically, the hybrid loss is based on the Huber loss, which combines the strengths of mean squared error (MSE) and mean absolute error (MAE). The first component of the hybrid loss function is the main reconstruction loss, defined as the Huber loss between the high-resolution ground truth \mathbf{Y}_{HR} and the model prediction \mathbf{Y}_{pred} :

$$\mathcal{L}_{rec} = \text{Huber}(\mathbf{Y}_{pred}, \mathbf{Y}_{HR}). \quad (6)$$

The second component is the spatial loss, defined as the Huber loss between the high-resolution ground truth \mathbf{Y}_{HR} and the Spatial-Net output $\mathbf{Y}_{pred,spatial}$:

$$\mathcal{L}_{spatial} = \text{Huber}(\mathbf{Y}_{pred,spatial}, \mathbf{Y}_{HR}). \quad (7)$$

In addition, the ground-truth image is decomposed into low- and high-frequency subbands using the discrete wavelet transform (DWT). The corresponding model outputs, \mathbf{Y}_L^{pred} and \mathbf{Y}_H^{pred} , are compared with their ground-truth counterparts, \mathbf{Y}_L and $\mathbf{Y}_H = [\mathbf{Y}_{LH}, \mathbf{Y}_{HL}, \mathbf{Y}_{HH}]$, to enforce accurate reconstruction across both frequency domains:

$$\mathcal{L}_{low} = \text{Huber}(\mathbf{Y}_L^{pred}, \mathbf{Y}_L), \quad \mathcal{L}_{high} = \text{Huber}(\mathbf{Y}_H^{pred}, \mathbf{Y}_H). \quad (8)$$

The total training objective combines all four components as

$$\mathcal{L}_{total} = \lambda_{rec} \mathcal{L}_{rec} + \lambda_{spatial} \mathcal{L}_{spatial} + \lambda_{low} \mathcal{L}_{low} + \lambda_{high} \mathcal{L}_{high}, \quad (9)$$

where the λ coefficients control the relative importance of the individual loss terms. This hybrid formulation encourages the network to produce spatially accurate reconstructions while enhancing edge sharpness and texture fidelity through frequency-domain supervision.

TABLE I: Ablation results of quantitative performance on the PaviaU dataset at scale 4 with model complexity.

Ablation Study		
Model Variant	MPSNR↑	SAM↓
Without Spatial-Net	30.218	4.932
Without Wavelet-Net	30.398	4.829
Without Shared Wavelet Branch	30.534	4.853
Without Band Grouping	30.524	4.731
Without Hybrid Loss	30.541	4.845
DDSRNet (Full Model)	30.561	4.836

Model Complexity		
Model	Scale	Parameters
ERCSR [17]	4x	1.59M
MCNet [18]	4x	2.17M
PDENet [19]	4x	2.30M
CSSFENet [13]	4x	1.61M
DDSRNet (Ours)	4x	0.07M

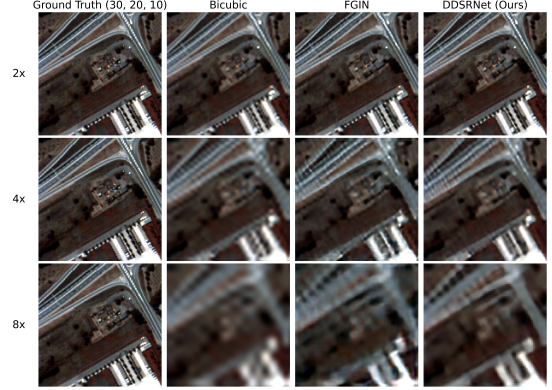


Fig. 2: Qualitative comparison on the PaviaU test image (false-color composite) at scaling factors of 2x, 4x, and 8x.

III. EXPERIMENTAL SETUP

A. Datasets

The performance of the model was evaluated on three benchmark hyperspectral datasets: Pavia Center (PaviaC) with 102 spectral bands, Pavia University (PaviaU) with 103 bands, and Chikusei, which provides a higher spectral resolution of 128 bands.

B. Implementation and Evaluation Metrics

To utilize the PaviaU and PaviaC datasets, training and testing samples for PaviaU and PaviaC were generated by extracting 144×144 patches, following [13]. In the Chikusei dataset, we first cropped a 512×512 region from the center of the image to exclude black areas. Subsequently, we extracted 64×64 patches for the 2x downscaling setting and 128×128 patches for the 4x downscaling setting, as suggested in [15]. Finally, all patches were downsampled with scale factors of 2x, 4x, and 8x, and the model was trained to reconstruct the original high-resolution images from these degraded inputs.

In addition, we extracted overlapping patches from the PaviaU dataset using a stride of 18×18 , while keeping non-overlapping patches for the other datasets. Spectral band grouping was applied with a group size of 35 without overlaps. We padded the training data to 105 channels by duplicating the last band as needed (e.g., three additional bands for PaviaC and two for PaviaU) to ensure equal channel sizes across datasets. For the Chikusei dataset, which originally contained

TABLE II: Evaluation on datasets (PaviaC, PaviaU) under different scaling factors. Results are reported from [13].

Scale Factor	Model	PaviaC			PaviaU		
		MPSNR \uparrow	MSSIM \uparrow	SAM \downarrow	MPSNR \uparrow	MSSIM \uparrow	SAM \downarrow
2 \times	VDSR [20]	34.87	0.9501	3.689	34.03	0.9524	3.258
	EDSR [21]	34.58	0.9452	3.898	33.98	0.9511	3.334
	MCNet [18]	34.62	0.9455	3.865	33.74	0.9502	3.359
	MSDformer [22]	35.02	0.9493	3.691	34.15	0.9553	3.211
	MSFMNet [23]	35.20	0.9506	3.656	34.98	0.9582	3.160
	AS3 ITransUNet [14]	35.22	0.9511	3.612	35.16	0.9591	3.149
	PDENet [19]	35.24	0.9519	3.595	35.27	0.9594	3.142
	CSSFENet [13]	35.52	0.9544	3.542	35.92	0.9625	3.038
	DDSRNet	36.39	0.9601	3.288	36.43	0.9550	2.921
4 \times	VDSR [20]	28.31	0.7707	6.514	29.90	0.7753	4.997
	EDSR [21]	28.59	0.7782	6.573	29.89	0.7791	5.074
	MCNet [18]	28.75	0.7826	6.385	29.99	0.7835	4.917
	MSDformer [22]	28.81	0.7833	5.897	30.09	0.7905	4.885
	MSFMNet [23]	28.87	0.7863	6.300	30.28	0.7948	4.861
	AS3 ITransUNet [14]	28.87	0.7893	5.972	30.28	0.7940	4.859
	PDENet [19]	28.95	0.7900	5.876	30.29	0.7944	4.853
	CSSFENet [13]	29.05	0.7961	5.816	30.68	0.8107	4.839
	DDSRNet	29.56	0.8232	5.542	30.56	0.8181	4.836
8 \times	VDSR [20]	24.80	0.4944	7.588	27.02	0.5962	7.133
	EDSR [21]	25.06	0.5282	7.507	27.46	0.6302	6.678
	MCNet [18]	25.09	0.5391	7.429	27.48	0.6254	6.683
	MSDformer [22]	25.21	0.5462	7.427	27.32	0.6341	6.668
	MSFMNet [23]	25.25	0.5464	7.449	27.58	0.6356	6.615
	AS3 ITransUNet [14]	25.25	0.5435	7.417	27.68	0.6413	6.574
	PDENet [19]	25.28	0.5436	7.402	27.73	0.6457	6.531
	CSSFENet [13]	25.35	0.5493	7.306	27.82	0.6569	6.505
	DDSRNet	25.57	0.5847	7.627	27.64	0.6250	6.770

TABLE III: Evaluation on the Chikusei dataset in different scaling setups. The comparison results are sourced from [15].

Scale	Model	MPSNR \uparrow	MSSIM \uparrow	SAM \downarrow
2 \times	Bicubic	35.008	0.932	1.718
	EDSR [21]	35.489	0.941	2.444
	GDRRN [24]	35.958	0.939	1.561
	SSPSR [25]	35.723	0.944	2.275
	MCNet [18]	36.371	0.948	1.784
	GELIN [26]	37.747	0.959	1.384
	DIFF [15]	38.748	0.966	1.638
	DDSRNet	38.406	0.963	1.044
4 \times	Bicubic	29.676	0.770	3.161
	EDSR [21]	29.976	0.799	4.127
	GDRRN [24]	30.658	0.801	2.913
	SSPSR [25]	30.858	0.823	3.196
	MCNet [18]	31.189	0.821	2.955
	GELIN [26]	31.095	0.838	2.834
	DIFF [15]	32.248	0.860	3.507
	DDSRNet	32.528	0.859	2.146

128 bands, we padded the data to 140 channels. During the evaluation, the padded channels were removed and only the original spectral bands were compared. For the PaviaU and PaviaC datasets, we adopted the same test patch as in [13]; in the case of the Chikusei dataset, the top left patch was used as the test set. The remaining patches were used for training and validation. The models were trained using Adam Optimizer with a learning rate of 0.0001 and a batch size of 4. Training was performed for up to 6000 epochs, with early stopping based on validation loss and patience of 200 epochs. A single-level Haar wavelet decomposition was applied to decouple spatial frequency components, and we allocated equal weights of 0.35 to each term in the hybrid loss function. As part of our evaluation of the test set, we applied widely used quantitative metrics, including Mean Peak Signal-to-Noise Ratio (MPSNR), Mean Structural Similarity Index (MSSIM), Spectral Angle Mapper (SAM), Root Mean Squared Error (RMSE), and Cross-Correlation (CC).

C. Ablation Study

We conducted an ablation study on the PaviaU dataset with a 4 \times downscaling factor to evaluate the individual contribution of each component in the proposed model. Table I summarizes

the results in terms of two HSI quality metrics, including MPSNR and SAM. We quantitatively evaluate the contribution of each component in both domains, such as Spatial-Net and Wavelet-Net. The replacement of Spatial-Net with a standard bilinear upsampling layer led to a significant drop in MPSNR by 0.343 dB and an increase in SAM by 0.096°. Removing the Wavelet-Net and directly using the Spatial-Net output as the final prediction also resulted in a decrease in MPSNR by 0.163 dB, although SAM decreased slightly by 0.007°. This highlights the advantage of frequency-domain processing. We further examined the effect of replacing the shared wavelet branch with independent branches for each high-pass subband, which negatively impacted all metrics.

Additionally, removing band grouping reduced MPSNR by 0.037 dB and increased model complexity, although it improved SAM by 0.105°. Finally, introducing the Hybrid Loss function led to a further improvement in MPSNR by 0.02 dB and a reduction in SAM error by 0.09°. When all components are integrated, the full DDSRNet model achieves the best overall performance, demonstrating the complementary effect of each module.

We further demonstrate the efficiency of the proposed model in terms of complexity. Specifically, DDSRNet requires only 0.07M parameters, which is significantly fewer than CSSFENet [13]. Figure 2 presents a qualitative comparison on the PaviaU test image among bicubic interpolation, FGIN [11], and the proposed DDSRNet. Under the challenging 8 \times scaling scenario, bicubic interpolation produces over-smoothed and blurred results, while FGIN preserves sharper structures but introduces mild aliasing artifacts. In contrast, DDSRNet effectively reconstructs fine edges and textures with fewer distortions. Overall, the proposed framework achieves an excellent trade-off between reconstruction accuracy and efficiency, making it well-suited for deployment in resource-constrained environments.

D. Comparison with State-of-the-Art Methods

The proposed DDSRNet model is evaluated on the PaviaC and PaviaU datasets under 2 \times , 4 \times , and 8 \times downscaling

factors, with quantitative results summarized in Table II, where DDSRNet shows superior performance under the $2\times$ setting. For the more challenging $4\times$ scaling factor, our model outperformed CSSFENet [13] on PaviaC, gaining 0.51 dB in MPSNR, 0.0271 in MSSIM, and reducing SAM by 0.274. On PaviaU, it showed similar performance to CSSFENet, with almost identical SAM and slightly higher MSSIM, while showing only a small drop of 0.12 dB in MPSNR. At the $8\times$ downscaling factor, DDSRNet had the highest MPSNR on PaviaC, surpassing CSSFENet by 0.22 dB, and showed better performance in MSSIM, while having a slightly higher SAM value than CSSFENet. On PaviaU, its performance was close to CSSFENet, with only minor differences (-0.18 dB in MPSNR, -0.0319 in MSSIM, and $+0.265$ in SAM).

Table III presents the experimental results across the $2\times$ and $4\times$ downscaling factors on the Chikusei dataset. At the $2\times$ scaling factor, DDSRNet achieved an MPSNR of 38.406 dB, which is 0.342 dB lower than the diffusion-based DIFF model [15], but higher than all other CNN-based models. DDSRNet also obtained an MSSIM of 0.963, nearly identical to the DIFF model's 0.966. In addition, it yielded a SAM value of 1.044. For the $4\times$ downscaling factor, DDSRNet achieved the highest MPSNR of 32.528 dB, outperforming the DIFF model by 0.28 dB, while producing a comparable MSSIM (0.859 vs. 0.860). Moreover, the SAM was reduced to 2.146, representing a decrease of 1.36 compared to the best reference method. These results confirm that DDSRNet outperforms recent approaches in addressing complex HSI super-resolution tasks.

IV. CONCLUSION

In this study, we introduced a dual-domain convolutional neural network for hyperspectral image super-resolution. The proposed architecture combines a Spatial-Net for initial feature extraction with a Discrete Wavelet Transform (DWT) module for frequency-domain refinement. In addition, a hybrid Huber loss-based loss function further enhances the reconstruction accuracy by jointly optimizing image, spatial and frequency domain components. Experimental results on three benchmark hyperspectral datasets demonstrate that our model achieves competitive reconstruction quality. In future work, we plan to extend the framework toward transformer-based or diffusion-driven dual-domain architectures to further improve generalization and efficiency across diverse hyperspectral imaging scenarios.

REFERENCES

- [1] X. Li, Y. Yuan, and Q. Wang, "Hyperspectral and multispectral image fusion based on band simulation," *IEEE Geoscience and Remote Sensing Letters*, vol. 17, no. 3, pp. 479–483, 2019.
- [2] L. Jiang, M. Zhong, and F. Qiu, "Single-image super-resolution based on a self-attention deep neural network," in *2020 13th International Congress on Image and Signal Processing, BioMedical Engineering and Informatics (CISP-BMEI)*. IEEE, 2020, pp. 387–391.
- [3] U. Muhammad, W. Wang, S. P. Chattha, and S. Ali, "Pre-trained vggnet architecture for remote-sensing image scene classification," in *2018 24th International Conference on Pattern Recognition (ICPR)*. IEEE, 2018, pp. 1622–1627.
- [4] U. Muhammad, W. Wang, A. Hadid, and S. Pervez, "Bag of words kaze (bowk) with two-step classification for high-resolution remote sensing images," *IET Computer Vision*, vol. 13, no. 4, pp. 395–403, 2019.
- [5] U. Muhammad, W. Wang, and A. Hadid, "Feature fusion with deep supervision for remote-sensing image scene classification," in *2018 IEEE 30th international conference on tools with artificial intelligence (ICTAI)*. IEEE, 2018, pp. 249–253.
- [6] U. Muhammad, M. Z. Hoque, W. Wang, and M. Oussalah, "Patch-based discriminative learning for remote sensing scene classification," *Remote Sensing*, vol. 14, no. 23, p. 5913, 2022.
- [7] Y. Chudasama, U. Muhammad, V. Mayra, F. Guiotte, and J. Laaksonen, "A comparison of hyperspectral super-resolution techniques for boreal forest imagery," in *IGARSS 2024-2024 IEEE International Geoscience and Remote Sensing Symposium*. IEEE, 2024, pp. 1226–1230.
- [8] U. Muhammad and J. Laaksonen, "Dacn: Dual-attention convolutional network for hyperspectral image super-resolution," *arXiv preprint arXiv:2506.05041*, 2025.
- [9] Z. Lai, Y. Fu, and J. Zhang, "Hyperspectral image super resolution with real unaligned rgb guidance," *IEEE Transactions on Neural Networks and Learning Systems*, vol. 36, no. 2, pp. 2999–3011, 2025.
- [10] U. Muhammad, J. Laaksonen, and L. Mihaylova, "Towards lightweight hyperspectral image super-resolution with depthwise separable dilated convolutional network," in *2025 IEEE Statistical Signal Processing Workshop (SSP)*, 2025, pp. 91–95.
- [11] U. Muhammad and J. Laaksonen, "A fusion-guided inception network for hyperspectral image super-resolution," in *2025 25th International Conference on Digital Signal Processing (DSP)*, 2025, pp. 1–5.
- [12] M. Usman and J. Laaksonen, "Hybrid deep learning for hyperspectral single-image super-resolution," *IEEE Geoscience and Remote Sensing Letters*, vol. 22, pp. 1–5, 2025.
- [13] J. Zhang, R. Zheng, Z. Wan, R. Geng, Y. Wang, Y. Yang, X. Zhang, and Y. Li, "Hyperspectral image super-resolution based on feature diversity extraction," *Remote Sensing*, vol. 16, no. 3, p. 436, 2024.
- [14] Q. Xu, S. Liu, J. Wang, B. Jiang, and J. Tang, "As 3 itransunet: Spatial-spectral interactive transformer u-net with alternating sampling for hyperspectral image super-resolution," *IEEE Transactions on Geoscience and Remote Sensing*, 2023.
- [15] Z. Wang, D. Li, M. Zhang, H. Luo, and M. Gong, "Enhancing hyperspectral images via diffusion model and group-autoencoder super-resolution network," in *Proceedings of the AAAI Conference on Artificial Intelligence*, vol. 38, no. 6, 2024, pp. 5794–5804.
- [16] Z. Lu, Q. Zou, F. Zhou, and Q. Liao, "Wavelet-based single image super-resolution with an overall enhancement procedure," in *2017 IEEE International Conference on Acoustics, Speech and Signal Processing (ICASSP)*. IEEE, 2017, pp. 1447–1451.
- [17] Q. Li, Q. Wang, and X. Li, "Exploring the relationship between 2d/3d convolution for hyperspectral image super-resolution," *IEEE Transactions on Geoscience and Remote Sensing*, vol. 59, no. 10, pp. 8693–8703, 2021.
- [18] L. Qiang, Q. Wang, and X. Li, "Mixed 2d/3d convolutional network for hyperspectral image super-resolution," *Remote sensing*, vol. 12, no. 10, p. 1660, 2020.
- [19] J. Hou, Z. Zhu, J. Hou, H. Zeng, J. Wu, and J. Zhou, "Deep posterior distribution-based embedding for hyperspectral image super-resolution," *IEEE Transactions on Image Processing*, vol. 31, pp. 5720–5732, 2022.
- [20] J. Kim, J. K. Lee, and K. M. Lee, "Accurate image super-resolution using very deep convolutional networks," in *Proceedings of the IEEE conference on computer vision and pattern recognition*, 2016, pp. 1646–1654.
- [21] B. Lim, S. Son, H. Kim, S. Nah, and K. Mu Lee, "Enhanced deep residual networks for single image super-resolution," in *Proceedings of the IEEE conference on computer vision and pattern recognition workshops*, 2017, pp. 136–144.
- [22] S. Chen, L. Zhang, and L. Zhang, "Msdformer: Multi-scale deformable transformer for hyperspectral image super-resolution," *IEEE Transactions on Geoscience and Remote Sensing*, 2023.
- [23] J. Zhang, M. Shao, Z. Wan, and Y. Li, "Multi-scale feature mapping network for hyperspectral image super-resolution," *Remote Sensing*, vol. 13, no. 20, p. 4180, 2021.
- [24] Y. Li, L. Zhang, C. Dingl, W. Wei, and Y. Zhang, "Single hyperspectral image super-resolution with grouped deep recursive residual network," in *2018 IEEE Fourth International Conference on Multimedia Big Data (BigMM)*. IEEE, 2018, pp. 1–4.
- [25] J. Jiang, H. Sun, X. Liu, and J. Ma, "Learning spatial-spectral prior for super-resolution of hyperspectral imagery," *IEEE Transactions on Computational Imaging*, vol. 6, pp. 1082–1096, 2020.
- [26] X. Wang, Q. Hu, J. Jiang, and J. Ma, "A group-based embedding learning and integration network for hyperspectral image super-resolution," *IEEE Transactions on Geoscience and Remote Sensing*, vol. 60, pp. 1–16, 2022.